RSC Advances

PAPER

View Article Online
View Journal | View Issue

Cite this: *RSC Adv.*, 2015, **5**, 5131

Gold-supported magnetically recyclable nanocatalysts: a sustainable solution for the reduction of 4-nitrophenol in water†

Mariana Rocha,[a] Carlos Fernandes,[a] Clara Pereira,*[a] Susana L. H. Rebelo,*[a] Manuel F. R. Pereira[b] and Cristina Freire*[a]

In this work mesoporous silica-coated manganese(II) ferrite ($MnFe_2O_4$) magnetic nanoparticles functionalized with amine and thiol groups were prepared and used as supports for the *in situ* immobilization of gold nanoparticles (Au NPs). The resulting Au-supported magnetic nanocatalysts, denoted as Mn@SiO_2_NH_2@Au and Mn@SiO_2_SH@Au, were tested in the reduction of 4-nitrophenol (4-NP) to 4-aminophenol (4-AP), at room temperature in water, in the presence of $NaBH_4$ reducing agent. This organic compound is typically used in the production of pesticides and dyes and commonly found in the resulting wastewaters. The chemical, morphological, textural and magnetic properties of the nanosupports and resulting Au-supported nanocatalysts were characterized by X-ray photoelectron spectroscopy, Fourier transform infrared spectroscopy, transmission electron microscopy, X-ray diffraction, N_2 adsorption–desorption isotherms at −196 °C and SQUID magnetometry. The influence of the type of organosilane linker between the magnetic nanosupport and the Au NPs on the *in situ* immobilization of the Au NPs was evaluated: Mn@SiO_2_NH_2@Au presented lower Au loading than Mn@SiO_2_SH@Au, but the anchored Au NPs showed a higher degree of crystallinity. The magnetic Au-supported nanocatalysts led to almost 100% reduction of 4-NP to 4-AP, monitored by UV-vis spectroscopy, with the reaction time depending on the type of nanocatalyst/linker: 12 and 17 min, for the amine- and thiol-based nanocatalysts respectively, what corresponded to pseudo first-order rate constants normalized for Au loading of K = 6117 $mmol^{-1}$ min^{-1} and 827 $mmol^{-1}$ min^{-1}, respectively. Both catalysts could be efficiently recovered by magnetic separation and were highly stable upon reuse in four further cycles, preserving their catalytic performance with negligible Au leaching.

Received 15th November 2014
Accepted 11th December 2014

DOI: 10.1039/c4ra15865b

www.rsc.org/advances

1. Introduction

In the last decades, nano-sized catalysts with large surface area to volume ratio have been recognized as very attractive alternatives to conventional catalysts, since they can provide substantial enhancements in catalytic activity, selectivity and stability.[1] However, their isolation and recovery from the catalytic reaction medium require the use of centrifugation/nanofiltration steps due to their nanometer size. These processes are often tiresome and inefficient to prevent catalyst losses, which hinders the sustainability and economic viability of the nanocatalysis approach. Magnetic-responsive nanomaterials have emerged as ideal intrinsic catalysts or catalyst supports since they can be isolated and recovered by magnetic separation, which is a more efficient and fast process when compared with centrifugation or filtration, avoiding catalyst mass losses or the use of additional solvents.[1]

Transition metal ferrites of MFe_2O_4-type, with M(II) being a 3d transition metal cation, are the most commonly employed magnetic nanoparticles (MNPs) for different applications,[2] because they are easy to synthesize, have high saturation magnetization M_S (with $MnFe_2O_4$ being the one that exhibits the highest M_S in bulk), and when their dimensions are reduced below a critical size they can exhibit superparamagnetic properties.[3] The combination of high M_S and superparamagnetism makes these nanomaterials very attractive, since they can be efficiently recovered from the reaction medium using a magnet and almost instantaneously redispersed upon the removal of the external applied magnetic field. Consequently, repeated cycles of separation and redispersion are possible because of the absence of "magnetic memory".

In order to use MNPs as catalyst supports, their surface coating constitutes a two-fold strategy to impart additional

[a]*REQUIMTE, Departamento de Química e Bioquímica, Faculdade de Ciências, Universidade do Porto, Rua do Campo Alegre, 4169-007, Porto, Portugal. E-mail: acfreire@fc.up.pt; clara.pereira@fc.up.pt; susana.rebelo@fc.up.pt; Fax: +351 220402659; Tel: +351 220402590; +351 220402576; +351 220402587*

[b]*Laboratório de Catálise e Materiais – Laboratório Associado LSRE/LCM, Faculdade de Engenharia, Universidade do Porto, 4200-465 Porto, Portugal*

† Electronic supplementary information (ESI) available. See DOI: 10.1039/c4ra15865b

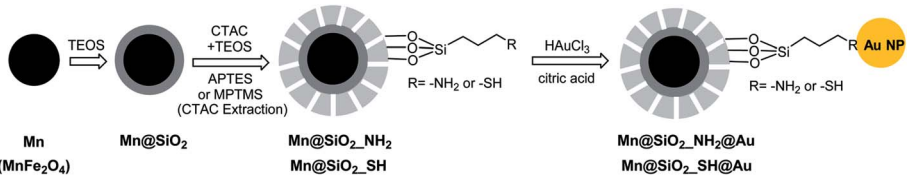

Scheme 1 Schematic representation of the nanocatalysts preparation.

advantages to the nanosupport: it allows the protection of the magnetic cores against degradation within the catalytic reaction medium (through dissolution and oxidation/reduction reactions) and facilitates the immobilization of the catalytic species by covalent strategies, without interfering with their superparamagnetic properties.[2] Silica is one of the most popular inorganic materials for the MNPs coating because it has high affinity to the MNPs surface, can have mesoporosity (which further increases the nanomaterial surface area) and contains surface Si–OH groups which can easily react with bifunctional organosilanes or other organic species containing various functional units.[4] In this context, the silica shell confers the possibility of immobilizing the catalytic active species on the nanomaterials surface through a variety of covalent strategies and can also improve the nanomaterial dispersibility in different reaction media.

Catalysis by gold nanoparticles (Au NPs) is a fast growing area within the field of metal-based nanocatalysis due to their unique physicochemical properties.[5] Colloidal gold has been reported as an active nanocatalyst for several types of reactions, in which reduction and oxidation reactions can be highlighted.[6,7] In particular, one of the most important reactions catalyzed by Au NPs is the reduction of 4-nitrophenol (4-NP), which is one of the most common organic pollutants found in industrial and agricultural wastewaters, typically used in the production of pesticides and dyes.[8,9] The reduction of this substrate by colloidal gold in the presence of $NaBH_4$ leads to the formation of 4-aminophenol (4-AP), which is a very important compound for a wide range of applications ranging from pharmaceuticals, corrosion treatments, among others.[8,9]

Despite the advantages of Au NPs, they present a great tendency to form aggregates in solution leading to the gradual decrease of their initial catalytic activity.[10] Furthermore, their high cost and limited supply are key obstacles for their application in catalytic technologies. Therefore, the immobilization of Au NPs onto different solid supports has been pursued aiming to improve the catalyst stability, avoid aggregation phenomenon and enable their recovery and recycling.[11,12] The deposition of Au NPs onto supports, such as graphene oxide,[13,14] carbon nanotubes,[15,16] polymers,[17,18] and oxides,[19–22] has been extensively explored.

Magnetic core–shell nanosupports have recently emerged as promising alternatives to prepare hybrid Au-based nanocatalysts.[23–26] In particular, magnetite (Fe_3O_4) has been the most used magnetic core for encapsulation within several types of shells such as polymers (the most common shell, *e.g.* polypeptides, polyethylenimine, polydopamine), carbon nanomaterials (reduced graphene oxide) and silica.[24] Although silica shell has been one of the prime choices for encapsulation of MNPs for subsequent functionalization and anchorage of several types of metallic nanoparticles or metal complexes with catalytic properties in oxidation and reduction reactions, scarce studies have been devoted to the use of silica-coated magnetic particles as supports for Au NPs, namely for the reduction of 4-NP.[26–28] Furthermore, the reported procedures are often time-consuming and complex, namely involving the previous synthesis of the Au NPs in a separate step, and/or leading to hierarchical assemblies or to micrometer sized gold-supported catalysts. In this context, the development of alternative less time-consuming routes (with lower number of steps) for the fabrication of magnetically-recyclable gold nanocatalysts is still highly desirable.

In this work, we prepared core-double shell magnetic nanosupports functionalized with amine and thiol groups for *in situ* immobilization of Au NPs (Scheme 1) with the ultimate goal of producing novel magnetically recyclable nanocatalysts for the reduction of 4-NP in water, in the presence of $NaBH_4$. The core-double shell nanosupports are composed by magnetic cores of manganese(II) ferrite ($MnFe_2O_4$, a nanoferrite with higher M_S value than that of Fe_3O_4 and superparamagnetic properties[29]) encapsulated in a silica double-shell structure that has been prepared by a two-step process. The two silica layers play the role of protection (non-porous inner shell) and provide large specific surface area (mesoporous outer shell) combined with surface $-NH_2$ or –SH functional groups to act as target points for Au NPs covalent immobilization. The influence of the type of organosilane linker between the magnetic nanosupport and the Au NPs on the *in situ* immobilization of the Au NPs and catalytic performance of the resulting nanocatalysts was evaluated. Hence, in this work a new strategy for the fabrication of magnetically-recyclable gold-supported nanocatalysts with superparamagnetic properties and high colloidal dispersibility in the catalytic reaction medium is proposed, based on the use of two distinct organosilanes as linking agents and on the one-pot *in situ* immobilization of Au NPs. The novelty of this approach lies on the use of organosilane linking agents to establish the covalent bonding between the nanosupport and the Au NPs and prevent the Au NPs leaching during the catalytic process. Additionally, and to the best of our knowledge, the influence of the type of linking agent (containing amine *versus* thiol groups) on the Au NPs immobilization efficiency, degree of crystallinity of the grafted Au and catalytic performance in the 4-NP reduction is for the first time addressed. Finally, a new type of superparamagnetic core with higher M_S value and less prone

to degradation phenomenon when compared with the traditionally used magnetite nanoparticles is used for the fabrication of magnetic nano-sized core-double shell silica supports. This work thus opens new avenues on the design of eco-sustainable gold-supported nanocatalysts for the degradation of wastewater organic pollutants.

2. Experimental section

2.1. Magnetic nanocatalysts preparation

(a) Preparation of the magnetic nanosupports. The $MnFe_2O_4$ nanoparticles were prepared by a coprecipitation methodology developed by us.[29] Typically, $MnCl_2 \cdot 4H_2O$ (10 mmol, Merck, ≥99%) was dissolved in 5 mL of an aqueous solution of HCl 1 : 4 v/v (Panreac, 37%) and $FeCl_3 \cdot 6H_2O$ (20 mmol, Merck, ≥98%) was dissolved in 40 mL of water. The solutions were heated and then quickly added to 200 mL of a 3.0 M aqueous solution of (±)-1-amino-2-propanol (MIPA, Sigma-Aldrich, 93%) previously heated at 100 °C. The reaction was kept under vigorous mechanical stirring for 2 h. The resulting material, denoted as Mn, was magnetically separated, washed with water and dried under vacuum at room temperature overnight.

To an aqueous dispersion (40 mL) of the as-prepared Mn (500 mg) nanoparticles, 200 mL of ethanol were added (Fisher Chemical, analytical grade) followed by sonication during 25 min. Then, 3 mL of NH_3 solution (28%, Analar Normapur) were added to the dispersion followed by the dropwise addition of 20 mL of an ethanolic solution of tetraethyl orthosilicate 5% v/v (TEOS, Fluka, ≥99%). The reaction mixture was vigorously stirred for 3 h. The resulting material, denoted as $Mn@SiO_2$, was separated by centrifugation, followed by four cycles of washing with ethanol (100 mL) alternated with magnetic separation to remove any excess of reagents and finally dried under vacuum at room temperature for 4 h.

The subsequent mesoporous silica coating with simultaneous organosilane functionalization was performed by a procedure adapted from ref. 30. The $Mn@SiO_2$ nanomaterial (175 mg) was dispersed in 74.5 mL of a mixture of water–ethanol (6 : 1 v/v) for 10 min. After that, 10.4 mL (7.865 mmol) of hexadecyltrimethylammonium chloride aqueous solution (CTAC, Sigma-Aldrich, 25 wt%) were added to the $Mn@SiO_2$ dispersion, followed by vigorous stirring over 10 min. Then, 1.8 mL (0.0136 mmol) of triethanolamine (TEA, Sigma-Aldrich, ≥99%) were added and the resulting dispersion was heated to 60 °C. To the reaction mixture, 1 mL of TEOS (4.48 mmol) and 0.1 mL of (3-aminopropyl)triethoxysilane (APTES, 0.427 mmol, Sigma-Aldrich, 99%) or (3-mercaptopropyl)trimethoxysilane (MPTMS, 0.538 mmol, Fluka, ≥97%) were added dropwise for 3 h and the reaction mixture was maintained under vigorous stirring for another 2 h. The obtained materials were centrifuged and then washed/magnetically separated four times with 150 mL of ethanol. For the removal of CTAC, the nanomaterials were refluxed with an ethanolic solution of ammonium nitrate (100 mL, 20 g L^{-1}, Merck, ≥98.5%) for 2 h. This procedure was repeated four times followed by reflux with ethanol (100 mL) for 2 h. The resulting materials, denoted as $Mn@SiO_2\_NH_2$ and $Mn@SiO_2\_SH$ for APTES and MPTMS functionalized core-double shell MNPs respectively, were magnetically separated and dried under vacuum at room temperature during 4 h.

(b) *In situ* decoration of functionalized nanosupports with gold NPs. Typically, the nanosupports $Mn@SiO_2\_NH_2$ and $Mn@SiO_2\_SH$ (50 mg) were dispersed in 30 mL of 2-propanol (Analar Normapur, analytical grade) by sonication. Then, 16 mg of $HAuCl_4 \cdot 3H_2O$ (0.05 mmol, Alfa Aesar, ≥49.0% Au basis) and 17 mg of citric acid (0.09 mmol, Sigma-Aldrich, ≥99.5%), both separately dissolved in 2-propanol (10 mL), were added simultaneously and dropwise to the nanosupport dispersions under vigorous stirring at room temperature. The resulting mixture was vigorously stirred at room temperature for 2 h. After that time, the materials were magnetically separated and washed once with 2-propanol (20 mL). Finally, the resulting nanomaterials were magnetically separated and dried under vacuum at room temperature for 2 h. The materials will be denoted as $Mn@SiO_2\_NH_2@Au$ and $Mn@SiO_2\_SH@Au$.

2.2. Physicochemical characterization

X-ray photoelectron spectroscopy (XPS) was performed at Centro de Materiais da Universidade do Porto (CEMUP, Porto, Portugal), in a VG Scientific ESCALAB 200A spectrometer using non-monochromatized Al Kα radiation (1486.6 eV). The powdered samples were pressed into pellets prior to the XPS studies. To correct possible deviations caused by electric charge of the samples, the C 1s band at 284.6 eV was taken as an internal standard. The XPS spectra were deconvoluted with the XPSPEAK 4.1 software, using non-linear least squares fitting routine after a Shirley-type background subtraction. The surface atomic percentages were calculated from the corresponding peak areas and by using the sensitivity factors provided by the manufacturer.

Fourier transform infrared spectra (FTIR) were collected with a Jasco FT/IR-460 Plus spectrophotometer in the 400–4000 cm^{-1} range using a resolution of 4 cm^{-1} and 32 scans. The spectra of the samples were obtained in KBr (99%, spectroscopic grade) pellets containing 0.6 wt% of sample.

Transmission electron microscopy (TEM) was performed at Departamento de Engenharia Cerâmica e do Vidro, Universidade de Aveiro (Aveiro, Portugal), with a Hitachi H-9000NA microscope operating at an accelerating voltage of 300 kV equipped with a nano-EDS from Rontec. The samples were dispersed in high-purity ethanol under sonication, after which a carbon-coated 400 mesh copper grid was immersed in the dispersion and then air-dried. A slight aggregation of the nanoparticles was observed due to magnetic interactions with the electron beam.

The nitrogen adsorption–desorption isotherms (−196 °C) were performed on a Quantachrome NOVA Surface Area and Pore Size analyzer. Surface area calculations were made using the Brunauer–Emmett–Teller (BET) equation.[31] The pore-size distributions were obtained by using non-local density functional theory (NLDFT) and applying the kernel file provided by Quantachrome's data reduction software, where a cylindrical-pore model was assumed.

Powder X-ray diffraction (XRD) measurements were performed at Departamento de Química, CQ-VR, Universidade de Trás-os-Montes e Alto Douro (UTAD, Vila Real, Portugal), at room temperature over the range $2\theta = 10–80°$ with a PW 3040/60 X'Pert Pro Röntgen diffractometer using Cu Kα radiation ($\lambda = 1.5406$ Å) and the Bragg–Brentano $\theta/2\theta$ configuration. The system includes the ultrafast PW3015/20 X'Celerator detector and a secondary monochromator.

The magnetic properties of the dried samples were studied at IFIMUP-IN, Physics and Astronomy Department, Faculty of Sciences of Porto University (FCUP, Porto, Portugal) using a commercial Quantum Design superconducting quantum interference device (SQUID) magnetometer. The magnetization (M) as a function of applied magnetic field (H) measurement was performed at 300 K with H up to 50 kOe.

2.3. Catalytic reduction of 4-NP

The catalytic reduction of 4-NP to 4-AP was carried out at room temperature on a quartz optical cell by monitoring the electronic spectra at 1 min intervals. The degradation of 4-NP was monitored by the absorbance decrease of the electronic band at $\lambda = 400$ nm due to nitrophenolate ion in basic media and development of a new electronic band at $\lambda = 300$ nm corresponding to the formation of 4-AP. A stock solution of 4-NP (0.05 mM, 1 L) containing K_2CO_3 (20 g) was prepared. For the study of reduction kinetics, 3 mL of 4-NP stock solution were transferred to the UV-Vis cell and 5.67 mg of $NaBH_4$ (0.15 mmol) were added. Upon addition of the reducing agent the electronic band at $\lambda = 400$ nm remained unaltered until addition of the gold-supported magnetic nanocatalyst Mn@SiO_2_NH_2@Au or Mn@SiO_2_SH@Au (3 mg). To test the reusability of both nanocatalysts, a 10 times scale up experiment was carried out in a 50 mL round bottom flask. In this case, the electronic spectra of the reaction mixtures were acquired at each 5 min by withdrawing 3 mL aliquots from the reaction medium. The reaction was stirred at controlled temperature (25 °C). After each catalytic cycle (reaction time of 12–16 min), the nanocatalysts were magnetically separated, washed once with water (50 mL) and then reused in a new cycle. This procedure was repeated up to 5 times and at the end of the reuse cycles, the materials were dried and characterized as described in the results and discussion section (Section 3). The materials after the catalytic studies were denominated as Mn@SiO_2_NH_2@Au_4NP and Mn@SiO_2_SH@Au_4NP.

Control experiments were performed with the nanosupports (Mn@SiO_2_NH_2 and Mn@SiO_2_SH) using the same catalytic reaction conditions. Adsorption of 4-NP substrate into the hybrid nanomaterials was also evaluated using similar catalytic reaction conditions, but in the absence of $NaBH_4$.

3. Results and discussion

3.1. Characterization of gold-supported magnetic nanocatalysts

Mesoporous silica-coated $MnFe_2O_4$ MNPs functionalized with amine and thiol groups were prepared and used as supports for the *in situ* immobilization of Au NPs. In order to confirm the successful preparation of the organosilane-functionalized magnetic nanosupports as well as the immobilization of the Au NPs on their surface, all the nanomaterials were characterized by XPS and the results are summarized in Tables 1 and S1 in the ESI.†

The Mn@SiO_2_NH_2 and Mn@SiO_2_SH nanomaterials are mainly composed of silicon and oxygen assigned to the silica matrix as well as small amounts of Mn and Fe from the magnetic cores (Table 1), suggesting the encapsulation of the MNPs with an external silica shell. Furthermore, the XPS results of both nanomaterials reveal the presence of carbon, as well as of the target elements nitrogen in the case of Mn@SiO_2_NH_2 and sulfur for Mn@SiO_2_SH, confirming the successful functionalization of the nanosupports with the organosilanes. A small amount of surface nitrogen is also detected in Mn@SiO_2_SH, which is probably due to a residual percentage of TEA or NH_4NO_3 used for the surfactant extraction.

In the case of Mn@SiO_2_NH_2, the N 1s high-resolution spectrum exhibits a band centered at 399.4 eV, which is assigned to the free amine groups from APTES organosilane, with a shoulder at 401.2 eV probably due to a slight protonation of the grafted amine species and/or to trace amounts of NH_4NO_3 used in the surfactant extraction step (Table S1 in the ESI†).[32] The S 2p high-resolution spectrum of Mn@SiO_2_SH sample, on the other hand, could be deconvoluted in two doublet bands, with each one being composed by S $2p_{3/2}$ and S $2p_{1/2}$ components. In the main doublet, the S $2p_{3/2}$ band at 163.3 eV is assigned to the –SH groups of MPTMS, whereas the S $2p_{3/2}$ component centered at 168.3 eV is ascribed to sulfonic $–SO_3H$ groups,[33] suggesting a slight sulfur oxidation during the nanomaterial preparation. For both nanomaterials, the C 1s region exhibits three components, with the main ones centered at

Table 1 Surface atomic percentages for magnetic nanomaterials obtained by XPS analysis[a]

	Atomic %							
Material	C 1s	O 1s	N 1s	Si 2p	Mn $2p_{3/2}$	Fe $2p_{3/2}$	S 2p	Au 4f
Mn@SiO_2_NH_2	13.16	59.00	2.86	22.33	0.49	2.17	—	—
Mn@SiO_2_NH_2@Au	15.12	58.53	2.83	22.51	0.28	0.69	—	0.04
Mn@SiO_2_SH	20.94	54.63	1.11	20.62	0.42	0.96	1.32	—
Mn@SiO_2_SH@Au	16.25	58.49	0.70	22.05	0.40	0.74	1.06	0.31

[a] Determined by the areas of the respective bands in the high-resolution XPS spectra.

284.6 and 286.3–286.5 eV which are assigned to C–H/C–C and C–O bonds, respectively, from the organosilanes.[32] Finally, the binding energies (BEs) of O 1s and Si 2p bands present the typical values of lattice oxygen and silicon in a silica framework. On the other hand, the BEs of the 2p doublets and corresponding satellite peaks of Mn 2p and Fe 2p regions are characteristic of Mn(II) and Fe(III) species, respectively, being in accordance with the expected oxidation states for $MnFe_2O_4$ ferrites prepared by aqueous coprecipitation.[32,34,35]

Upon the immobilization of Au NPs in the two magnetic nanosupports, the target element gold is detected in both Mn@SiO_2_NH_2@Au and Mn@SiO_2_SH@Au samples (Table 1), confirming their successful incorporation. The Au surface atomic percentages are 0.04% for Mn@SiO_2_NH_2@Au and 0.31% for Mn@SiO_2_SH@Au, corresponding to 0.02 and 0.16 mmol g^{-1}, respectively. In this context, Mn@SiO_2_SH@Au contains a higher amount of gold grafted on its surface than Mn@SiO_2_NH_2@Au, which suggests that although both organosilanes are efficient linking agents to anchor Au NPs to the magnetic silica-coated support, the one containing thiol groups presents higher affinity for gold.

This fact is also sustained through the analysis of the S 2p and N 1s BEs for Mn@SiO_2_SH@Au and Mn@SiO_2_NH_2@Au, respectively (Table S1 in the ESI†). The immobilization of Au NPs onto the mercapto-functionalized nanosupport leads to a shift of the S $2p_{3/2}$ band from –SH groups to a lower value (0.6 eV shift), very close to that of the S $2p_{3/2}$ band associated with S–Au bonds which typically occurs at 162 eV.[36] These results are an indication of the formation of a covalent bond between the thiol groups from the nanosupport and gold. The BE of the S $2p_{3/2}$ band corresponding to $-SO_3H$ groups is also 0.5 eV lower than that of the parent nanosupport, suggesting that these groups also interact with the Au NPs. In the case of Mn@SiO_2_NH_2@Au, no significant changes are observed in the BEs of the N 1s bands when compared with those of the parent amine-functionalized support probably due to its lower Au surface loading.

The high-resolution Au 4f spectra of both Au-based nanomaterials can be deconvoluted in two components with BEs of 84.2–84.5 and 87.9–88.2 eV which are respectively assigned to Au $4f_{7/2}$ and Au $4f_{5/2}$ bands from metallic gold, confirming the reduction of Au(III) to Au(0) during the *in situ* immobilization step.[37,38] This is also sustained by the absence of the Au 4f doublet from Au(III) which typically occurs at 86.9 and 90.6 eV (for Au $4f_{7/2}$ and Au $4f_{5/2}$, respectively), demonstrating that the Au(III) from $HAuCl_3$ was completely reduced.[38,39]

To provide further insights on the chemical design of the magnetic nanosupports, the parent Mn nanoparticles before and after the coating with the silica shells and functionalization with the organosilanes were characterized by FTIR spectroscopy. In the FTIR spectrum of the parent Mn sample (Fig. S1 in the ESI†) is detected a strong band around 577 cm^{-1} which is assigned to M–O (M = Mn(II), Fe(III)) stretching vibrations of the manganese(II) ferrite lattice.[29] The coating of the Mn nanoparticles with a silica shell leads to the appearance of new bands in the FTIR spectrum of Mn@SiO_2 sample, namely at 1088 cm^{-1} with a shoulder around ~1200 cm^{-1} related to Si–O–Si asymmetric stretching vibrations, at 802 and 464 cm^{-1} ascribed to Si–O–Si symmetric stretching and bending modes, respectively, and at 948 cm^{-1} due to Si–O stretching vibrations of Si–OH and $Si–O^-$ groups.[34,40,41] These bands thus confirm the successful coating of the MNPs with a silica shell. Additionally, the spectrum presents a broad band at 3430 cm^{-1} from O–H stretching vibrations of surface silanol groups and physically adsorbed water,[42] and a band at 1620 cm^{-1} assigned to H–O–H bending vibrations of adsorbed water.[34,43]

Upon the Mn@SiO_2 coating with a porous silica shell and simultaneous functionalization with the organosilanes – samples Mn@SiO_2_NH_2 and Mn@SiO_2_SH – several new bands can be observed in the corresponding FTIR spectra: in the range of 2925–2856 cm^{-1} assigned to $-CH_3$ and $-CH_2$ asymmetric and symmetric stretching modes, at 1414 cm^{-1} due to C–H bending vibrations of methylene groups and at 1383 cm^{-1} assigned to $-CH_2$ wagging vibrations,[44] indicating the successful incorporation of the organosilanes,[45] in accordance with XPS. Nevertheless, the sharp peak at 1383 cm^{-1} which appears in both spectra may also have a contribution from the residual amount of NH_4NO_3 used in the surfactant extraction step.[46]

The FTIR spectrum of the Mn@SiO_2_NH_2 sample shows an extra band at 1510 cm^{-1} assigned to symmetric $-NH_2$ bending vibrations from the grafted APTES.[43] In the case of Mn@SiO_2_SH, the band related to S–H stretching vibrations which occurs in the range of 2600–2540 cm^{-1} could not be observed since it presents weak (and sometimes very weak) intensity, limiting its detection by FTIR.[46] Finally, an increase of the intensity of the bands corresponding to Si–O and O–H stretching and bending vibrations as well as a broadening of the latter can be observed, confirming the increase of the silica shell thickness ongoing from Mn@SiO_2 to the organosilane-functionalized nanosupports.

The TEM images of Mn@SiO_2_NH_2 and Mn@SiO_2_SH nanoparticles (Fig. 1a.1 and S2a.1 in the ESI†) confirm the core–shell morphology of the nanomaterials with average particle sizes of 164 ± 23 nm and 193 ± 16 nm, respectively, revealing that the Mn@SiO_2_NH_2 nanoparticles present smaller size and silica shell thickness than the mercapto-based counterpart, with the latter nanosupport showing some degree of aggregation. For both nanomaterials, each core–shell nanoparticle contains multiple magnetic cores surrounded by a porous silica shell with a nearly spherical morphology and a wormhole-type pore arrangement.[47]

The TEM characterization also confirms the presence of Au NPs immobilized on the surface of the Mn@SiO_2_NH_2@Au sample, with an average particle size of 5 ± 1 nm (Fig. 1a.2). In the case of Mn@SiO_2_SH@Au, the Au NPs could not be visually observed probably due to silica aggregation or because gold is present in an amorphous phase (Fig. S2a.2 in the ESI†). However, the EDS analysis (Fig. S2b.2 in the ESI†) confirms the existence of gold in this sample in accordance with XPS, which suggests that the grafted Au NPs present low crystallinity. For all the samples, the EDS analysis (Fig. 1b.1 and b.2, S2b.1 and b.2 in the ESI†) certifies the chemical composition provided by XPS, sustaining the successful incorporation of the organosilanes and Au NPs.

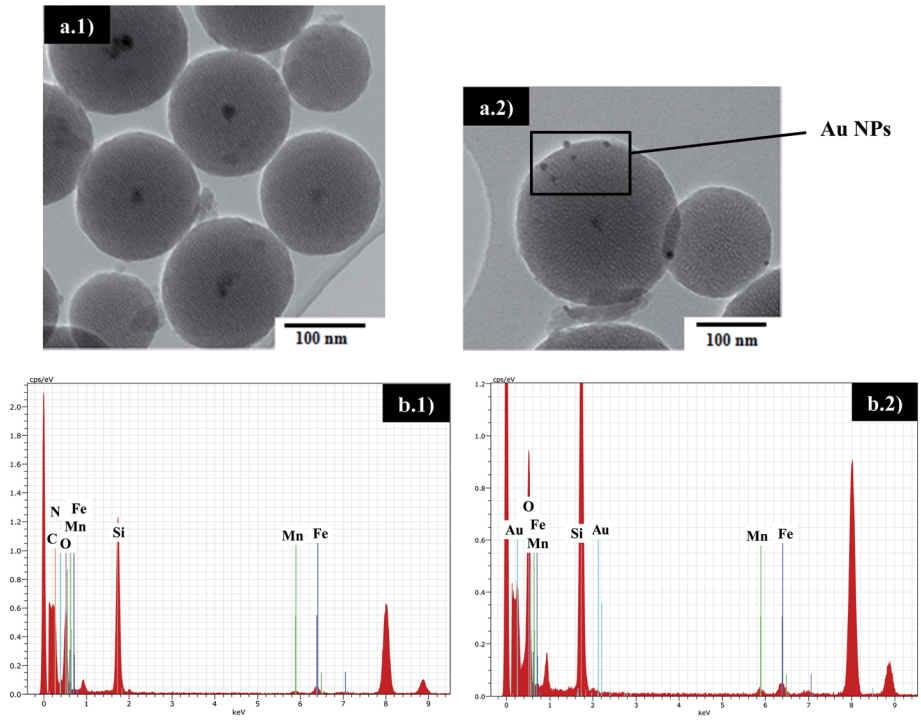

Fig. 1 TEM micrographs of (a.1) Mn@SiO_2_NH_2 and (a.2) Mn@SiO_2_NH_2@Au and EDS spectra of (b.1) Mn@SiO_2_NH_2 and (b.2) Mn@SiO_2_NH_2@Au.

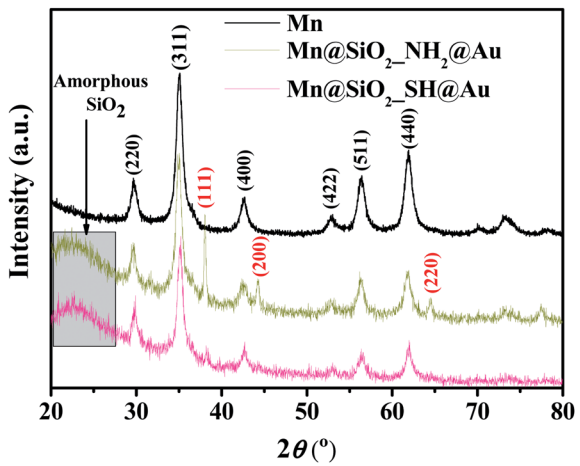

Fig. 2 Wide angle X-ray diffractograms of samples Mn, Mn@SiO_2_NH_2@Au and Mn@SiO_2_SH@Au.

XRD technique was also used to confirm the presence and structure of the Au NPs grafted to the magnetic nanosupports surface. In the XRD patterns of Mn@SiO_2_NH_2@Au and Mn@SiO_2_SH@Au samples (Fig. 2) are detected three diffraction peaks at $2\theta = 38.1$, 44.4 and 64.5° which are assigned to the (111), (200) and (220) Bragg reflections of gold with a face centered cubic structure (JCPDS card 04-0784).[48,49] However, in the case of Mn@SiO_2_SH@Au, those reflections are significantly weaker, suggesting the low crystallinity of the Au NPs, thus corroborating the TEM results.

Furthermore, the diffractograms of both samples exhibit additional peaks which match well those of the parent manganese(II) ferrite with a spinel-type cubic structure (space group *Fd3m*, JCPDS card 88-1965 for bulk $MnFe_2O_4$),[29] confirming that the structure of the magnetic cores is preserved after the coatings and immobilization procedures. Finally, a broad band around $2\theta = 22.2°$ is observed, which is assigned to the amorphous silica shell.[50]

The porous nature of the magnetic nanosupports was further confirmed by N_2 adsorption–desorption isotherms at −196 °C (Fig. 3a), which are of type IV, being characteristic of mesoporous materials.[47]

The specific surface area (A_{BET}) of Mn@SiO_2_SH sample is higher than that of Mn@SiO_2_NH_2 despite the pore volume and pore diameter values being practically similar (Table 2 and Fig. 3b). Additionally, in the case of the APTES-functionalized sample the pore size distribution is slightly broader, suggesting that the induction of porosity was more efficient using the organosilane MPTMS. These differences are probably related with the different acidity and hydrophobicity of the grafted organosilane (weakly acidic and relatively hydrophobic MPTMS *versus* basic and hydrophilic APTES).[47,51] According to the work of Bein and co-authors,[47] organosilanes bearing more hydrophobic functionalities can align themselves with the surfactant hydrophobic organic tails, while more hydrophilic residues have the opposite effect.

In order to evaluate the potentiality of Mn@SiO_2_NH_2 and Mn@SiO_2_SH as magnetically recyclable nanosupports for the immobilization of Au NPs, their magnetic properties at room temperature (300 K) were studied by SQUID magnetometry. The

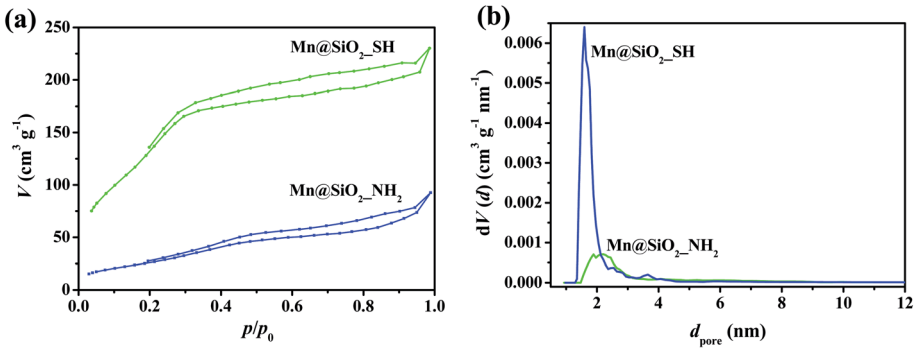

Fig. 3 (a) Nitrogen adsorption–desorption isotherms at −196 °C and (b) NLDFT pore size distributions of Mn@SiO_2_NH_2 and Mn@SiO_2_SH nanomaterials.

Table 2 Textural and magnetic properties (at 300 K) of the samples functionalized with APTES and MPTMS

	N_2 adsorption data			Magnetic properties
Sample	A_{BET} (m^2 g^{-1})	V_{pore}[a] (cm^3 g^{-1})	d_{pore}[b] (nm)	M_S[c] (emu g^{-1})
Mn@SiO_2_NH_2	105	0.111	4.41	12.6
Mn@SiO_2_SH	492	0.107	3.17	12.2

[a] Pore volume at p/p_0 = 0.98. [b] Pore diameter determined by DFT method (maximum of the NLDFT pore size distribution). [c] Saturation magnetization at 300 K.

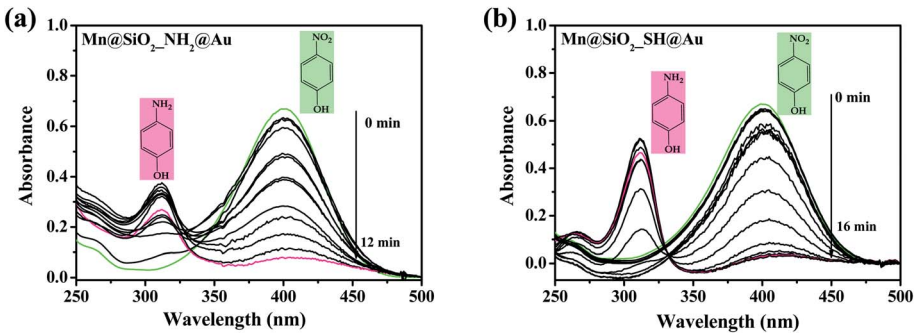

Fig. 4 Time-dependent UV-Vis spectra of the 4-NP reduction catalyzed by the magnetic nanomaterials (a) Mn@SiO_2_NH_2@Au and (b) Mn@SiO_2_SH@Au.

magnetization as a function of applied magnetic field at 300 K, *i.e.* $M(H)$ curves, of Mn@SiO_2_NH_2 and Mn@SiO_2_SH (Fig. S3 in the ESI†) reveal that the magnetic nanosupports are superparamagnetic at room temperature (coercive fields in the range of 6.6–6.9 Oe, well below 20 Oe), thus preserving the superparamagnetic properties of the parent Mn cores. As expected, the saturation magnetization (M_S) values of Mn@SiO_2_NH_2 and Mn@SiO_2_SH at 300 K (12.6 and 12.2 emu g^{-1}, respectively, Table 2) are lower than those of the parent magnetic cores (57.8 emu g^{-1}) and of Mn@SiO_2 (35.4 emu g^{-1}), confirming the presence of the diamagnetic silica matrix and the increase of the silica shell thickness from the first to the second silica coating. Furthermore, the M_S value of Mn@SiO_2_NH_2 is slightly higher than that of Mn@SiO_2_SH sample due to the presence of a thinner silica shell.

Although the M_S values of the magnetic nanosupports are lower than those of the parent Mn and Mn@SiO_2 samples, they are still high enough to allow their fast and efficient magnetic separation from the reaction medium by application of an external magnetic field. In this context, they will facilitate the catalyst recovery after the catalytic tests. Additionally, their superparamagnetic properties, *i.e.* absence of "magnetic memory", are of utmost importance to ensure the immediate redispersion of the magnetic nanocatalyst particles in the reaction medium after removal of the applied magnetic field.

3.2. Catalytic degradation of 4-NP

The catalytic performance of the magnetic nanocatalysts Mn@SiO_2_NH_2@Au and Mn@SiO_2_SH@Au was evaluated in the reduction of 4-NP in water in the presence of $NaBH_4$. The

catalytic reactions were monitored by UV-Vis spectroscopy, by recording the UV spectra of aliquots withdrawn from the reaction medium at 1 min intervals (more details in Section 2.3). In Fig. 4 are presented the time-dependent UV-Vis spectra of the 4-NP reduction catalyzed by both nanocatalysts.

As shown in Fig. 4a and b, upon the increase of the reaction time, the intensity of the absorption band at $\lambda \sim 400$ nm from 4-nitrophenolate ion becomes weaker and, at the same time, an absorption band around $\lambda = 300$ nm appears due to the formation of 4-AP, which increases in intensity during the course of the reaction.[26] The 4-NP reduction could also be confirmed by visual inspection, through the gradual fading of the bright yellow color of the reaction medium until complete color disappearance.

Both hybrid nanocatalysts are highly active in the 4-NP reduction, with the reaction catalyzed by Mn@SiO_2_NH_2@Au reaching the maximum substrate conversion of 97.2% within 12 minutes, whereas for the reaction catalyzed by Mn@SiO_2_SH@Au the maximum conversion of 96.7% was achieved after 16 minutes of reaction time.

The kinetic profiles of the 4-NP reduction using both nanocatalysts are presented in Fig. 5, through the representation of $\ln(A_t/A_0)$ as a function of the reaction time, where A_t and A_0 are the absorbance of 4-NP at times t and 0 min, respectively.

From Fig. 5 it can be observed that upon the addition of the Mn@SiO_2_SH@Au catalyst, a certain period of time, known as induction period, t_0, of 9 minutes, is required for the reduction reaction to start (dashed rectangle in Fig. 5). The induction period is usually observed in the catalytic reduction of 4-NP by metallic nanoparticles and has been interpreted in terms of the time needed for the substrate and reducing species to diffuse/adsorb to the surface of the nanoparticles and concomitant restructuring of the nanoparticles surface.[52,53] For Mn@SiO_2_NH_2@Au no induction period is observed, with the reduction reaction starting immediately upon the addition of the nanocatalyst; nevertheless, two reaction rate profiles are clearly observed, with the reaction rate in the first 6 minutes being much lower than that exhibited after the seventh minute. The existence of the induction period for Mn@SiO_2_SH@Au may be justified by the distinct textural properties of the nanomaterials: although Mn@SiO_2_SH@Au presents a higher surface area than the APTES-based counterpart (4.7 times higher), it shows a higher degree of agglomeration and probably a lower degree of Au crystallinity, as suggested by TEM and XRD, that can delay the reactants adsorption/diffusion step and Au surface reconstruction needed for the reduction reaction at the gold surface.

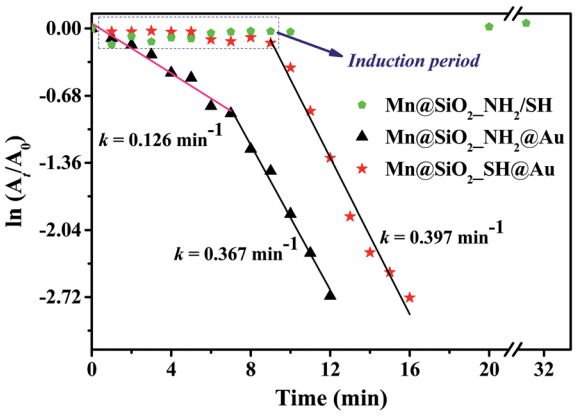

Fig. 5 Pseudo-first order plots of 4-NP reduction catalyzed by Mn@SiO_2_SH@Au and Mn@SiO_2_SH@Au, in the presence of $NaBH_4$. For comparison the plots of 4-NP reduction using the magnetic nanosupports are also presented.

For Mn@SiO_2_SH@Au, after the induction period of 9 minutes the reduction reaction starts and the $\ln(A_t/A_0)$ as a function of the reaction time plot presents a linear behavior. In the case of Mn@SiO_2_NH_2@Au, a linear behavior is observed for all the reaction period but with two distinct slopes (as referred above).

In the experimental conditions used, the reduction rate is independent of $NaBH_4$ concentration (excess amount of $NaBH_4$ was used) and, consequently, the reduction reactions can be considered as being of pseudo-first-order. In this context, the pseudo-first-order rate constants, k, were calculated from the slopes of the linear ranges of the $\ln(A_t/A_0) = -kt$ plots and are summarized in Table 3. The k values for Mn@SiO_2_SH@Au and Mn@SiO_2_NH_2@Au (in this latter case, extracted from the steepest slope) are almost similar, 0.367 min^{-1} and 0.397 min^{-1}, respectively. As previously referred, the reaction catalyzed by Mn@SiO_2_NH_2@Au also exhibits a second k value with lower value (0.126 min^{-1}), which is associated with the first 6 minutes of reaction. The lower reaction rate in the first minutes can be due to a competition between substrate reduction *versus* substrate/$NaBH_4$ adsorption in the nanocatalyst surface.

A more accurate comparison between the catalytic activity of the nanocatalysts can be performed by normalizing the k values to the amount of gold on each nanocatalyst. In this context, a second constant K was determined, normalizing the k values to the gold surface contents determined by XPS. The K value (presented in Table 3) is significantly higher in the case of Mn@SiO_2_NH_2@Au (6117 $mmol^{-1}$ min^{-1}) than for the MPTMS-based counterpart (827 $mmol^{-1}$ min^{-1}), indicating that the former presents a higher catalytic performance albeit its lower Au loading. Although no information could be obtained on the relative size of the Au NPs in the two nanosupports, the lower catalytic activity of Mn@SiO_2_SH@Au may be related to differences in the crystallinity degree of the gold supported nanoparticles and/or to the degree of aggregation of the nanocatalyst in the reaction medium. Compared with the literature,[1,37] the synthesized nanocatalysts, exhibited comparable or better catalytic activity for 4-NP reduction.

The magnetic nanosupports Mn@SiO_2_NH_2 and Mn@SiO_2_SH were also tested as catalysts in the 4-NP reduction, revealing no catalytic activity, since no changes in the UV-Vis absorption spectra of the reaction media were observed after one week of reaction (Fig. 5 and S4 in the ESI†). These features also confirm that the catalytic activity of Mn@SiO_2_NH_2@Au and Mn@SiO_2_SH@Au nanomaterials is due to the grafted Au NPs. Furthermore, substrate adsorption tests were performed with the gold-based magnetic nanocatalysts without the addition of $NaBH_4$ (not shown), revealing only a slight adsorption of

Table 3 Catalytic parameters for the 4-NP reduction catalyzed by the Au-based nanomaterials[a]

Sample	t^b (min)	$t_0{}^c$ (min)	k^d (min^{-1})	K^e (min^{-1} $mmol^{-1}$)
$Mn@SiO_2\_NH_2@Au$	12	0	0.126 ± 0.009, ($r^2 = 0.9636$) 0.367 ± 0.017, ($r^2 = 0.9898$)	6117
$Mn@SiO_2\_SH@Au$	16	9	0.397 ± 0.022, ($r^2 = 0.9798$)	827

[a] Reactions performed with 3 mL of 0.05 mM 4-NP aqueous solution and 3 mg of nanocatalyst. [b] Reaction time to achieve maximum 4-NP conversion to 4-AP. [c] Induction period. [d] Determined from the slope of $\ln(A_t/A_0) = -kt$ plots. [e] K was calculated as $K = k\ (min^{-1})/n_{Au}$ (mmol).

4-NP on the nanocatalysts (~6% after 18 h), and thus certifying that the decrease of the intensity of the absorption band at $\lambda \sim 400$ nm from 4-nitrophenolate ion during the catalytic reaction is due to its reduction to 4-aminophenolate ion.

To evaluate the recyclability of the as-prepared magnetic nanocatalysts, $Mn@SiO_2\_NH_2@Au$ and $Mn@SiO_2\_SH@Au$, they were separated from the reaction medium by magnetic decantation and reused in 4 further cycles. Both nanocatalysts preserved their catalytic performance in terms of reaction time and 4-NP conversion (97.5–100% and 96.5–98.8% for $Mn@SiO_2\_NH_2@Au$ and $Mn@SiO_2\_SH@Au$, respectively), without any loss of efficiency after five cycles, indicating their excellent catalytic activity and stability upon reuse (Fig. 6).

After the five consecutive cycles, the magnetic nanocatalysts were further characterized by FTIR and XPS. The FTIR spectra of $Mn@SiO_2\_NH_2@Au$ and $Mn@SiO_2\_SH@Au$ after the recycling tests (Fig. S5 in the ESI†) do not exhibit significant changes when compared with the FTIR spectra of the original magnetic nanocatalysts, which confirms that their structure is preserved upon recycling and reuse.

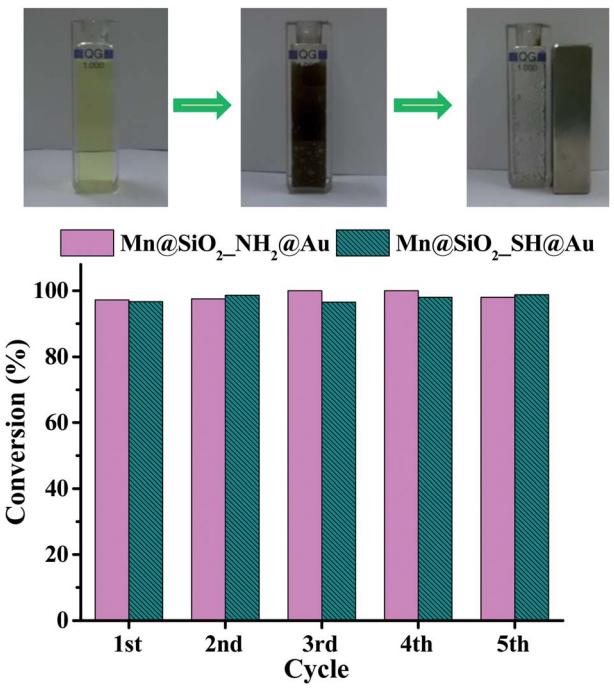

Fig. 6 Recycling tests performed with the magnetic nanocatalysts $Mn@SiO_2\_NH_2@Au$ and $Mn@SiO_2\_SH@Au$ in the reduction of 4-NP using $NaBH_4$ as reducing agent.

The Au surface content after the catalytic tests was quantified by XPS revealing that the Au percentage remains practically unchanged. In the case of $Mn@SiO_2\_NH_2@Au$, the Au atomic percentage is 0.04% which is equal to the value obtained before catalysis and in the case of $Mn@SiO_2\_SH@Au$ there is only a slight decrease of the atomic percentage (from 0.31 to 0.28%). These results indicate that the gold leaching upon the nanocatalysts recycling and reuse in five cycles is almost negligible, confirming the robustness of the nanocatalysts upon reuse.

4. Conclusions

Magnetic core-double shell silica nanosupports functionalized with amine and thiol groups, $Mn@SiO_2\_NH_2$ and $Mn@SiO_2\_SH$, were successfully prepared and used for the *in situ* immobilization of Au NPs: the former nanosupport allowed the immobilization of 5 nm crystalline Au NPs, whereas for $Mn@SiO_2\_SH$, TEM/EDS and XRD suggested the presence of less crystalline Au. Furthermore, the nanosupport functionalized with the organosilane with more hydrophilic character (containing $-NH_2$ groups) dispersed better in the catalytic reaction medium (water-based medium), despite bearing weaker target sites for Au NPs immobilization, since a lower Au content was observed by XPS for $Mn@SiO_2\_NH_2@Au$ when compared to $Mn@SiO_2\_SH@Au$.

Both $Mn@SiO_2\_NH_2@Au$ and $Mn@SiO_2\_SH@Au$ showed very good catalytic activity in the reduction of 4-NP to 4-AP (substrate conversion of 96.7–97.2%), with K values (corresponding to k normalized for Au content) significantly higher for the $Mn@SiO_2\_NH_2@Au$ nanocatalyst (6117 $mmol^{-1}$ min^{-1}) than for the MPTMS-based counterpart (827 $mmol^{-1}$ min^{-1}). Although no information could be obtained on the relative size of the Au NPs grafted to the two nanosupports, the lower catalytic activity of $Mn@SiO_2\_SH@Au$ may be related to differences in the crystallinity degree of the gold supported nanoparticles and/or to the degree of aggregation of the nanocatalyst. The two nanosupports showed superparamagnetic properties, that allowed their easy separation from the reaction media by application of an external magnetic field and the immediate redispersion in a new reaction medium after removal of the applied magnetic field. Finally, both nanocatalysts could be reused in four further cycles, preserving or slightly increasing their catalytic performance with negligible or no Au leaching, showing that the organosilane-functionalized silica nanoparticles containing magnetic MnF_2O_4 cores are an attractive alternative as magnetic nanosupports for the immobilization of Au NPs for catalytic applications.

Acknowledgements

This work was funded by Fundação para a Ciência e a Tecnologia (FCT) and FEDER, through grants no. PEst-C/EQB/LA0006/2013, FCOMP-01-0124-FEDER-037285 and Operation NORTE-07-0124-FEDER-000067-Nanochemistry. The authors thank Prof. P. Tavares and MSc. L. Fernandes from UTAD (Vila Real, Portugal) for the XRD measurements and Prof. J. P. Araújo from IFIMUP-IN, FCUP (Porto, Portugal) for access to the SQUID magnetometer. M. Rocha also thanks FCT for a PhD grant (SFRH/BD/52529/2014).

References

1 L. M. Rossi, N. J. S. Costa, F. P. Silva and R. Wojcieszak, *Green Chem.*, 2014, **16**, 2906–2933.
2 (*a*) A.-H. Lu, E. L. Salabras and F. Schüth, *Angew. Chem., Int. Ed.*, 2007, **46**, 1222–1244; (*b*) J. Gallo, N. J. Long and E. O. Aboagye, *Chem. Soc. Rev.*, 2013, **42**, 7816–7833.
3 Y.-W. Jun, J.-W. Seo and J. Cheon, *Acc. Chem. Res.*, 2008, **41**, 179–189.
4 I. Slowing, J. L. Vivero-Escoto, B. G. Trewyn and V. S.-Y. Lin, *J. Mater. Chem.*, 2010, **20**, 7924–7937.
5 M.-C. Daniel and D. Astruc, *Chem. Rev.*, 2004, **104**, 293–346.
6 G. C. Bond, C. Louis and D. T. Thompson, *Catalysis by Gold*, Imperial College Press, London, United Kingdom, 2006.
7 A. Stephen, K. Hashmia and G. J. Hutchings, *Catal. Sci. Technol.*, 2013, **3**, 2861.
8 L. Dykmana and N. Khlebtsov, *Chem. Soc. Rev.*, 2012, **41**, 5577–5587.
9 S. S. Kundu, M. Mandal, S. K. Ghosh and T. Pal, *J. Colloid Interface Sci.*, 2004, **272**, 134–144.
10 K. E. Peceros, X. Xu, S. R. Bulcock and M. B. Cortie, *J. Phys. Chem. B*, 2005, **109**, 21516–21520.
11 M. Zhao, L. Sun and R. M. Crooks, *J. Am. Chem. Soc.*, 1998, **120**, 4877–4878.
12 C. Zhu, L. Han, P. Hu and S. Dong, *Nanoscale*, 2012, **4**, 1641–1646.
13 X. Zhou, X. Huang, X. Qi, S. Wu, C. Xue, F. Y. C. Boey, Q. Yan, P. Chen and H. Zhang, *J. Phys. Chem. C*, 2009, **113**, 10842–10846.
14 J. Huang, L. Zhang, B. Chen, N. Ji, F. Chen, Y. Zhang and Z. Zhang, *Nanoscale*, 2010, **2**, 2733–2738.
15 X. Hu, T. Wang, X. Qu and S. Dong, *J. Phys. Chem. B*, 2006, **110**, 853–857.
16 H. Li, J. K. Jo, L. Zhang, C.-S. Ha, H. Suh and I. Kim, *Adv. Funct. Mater.*, 2010, **20**, 3864–3873.
17 G. L. Li, L. Q. Xu, K. G. Neoh and E. T. Kang, *Macromolecules*, 2011, **44**, 2365–2370.
18 S. Wunder, F. Polzer, Y. Lu, Y. Mei and M. Ballauff, *J. Phys. Chem. C*, 2010, **114**, 8814–8820.
19 Z. W. Seh, S. Liu, M. Low, S.-Y. Zhang, Z. Liu, A. Mlayah and M.-Y. Han, *Adv. Mater.*, 2012, **24**, 2310–2314.
20 H. Gu, J. Wang, Y. Ji, Z. Wang, W. Chen and G. Xue, *J. Mater. Chem. A*, 2013, **1**, 12471–12477.
21 M. Haruta, *Catal. Surv. Jpn.*, 1997, **1**, 61–73.
22 M. Haruta, *CATTECH*, 2002, **6**, 102–115.
23 T. Cheng, D. Zhang, H. Li and G. Liu, *Green Chem.*, 2014, **16**, 3401–3427.
24 D. Wang and D. Astruc, *Chem. Rev.*, 2014, **114**, 6949–6985.
25 V. Polshettiwar, R. Luque, A. Fihri, H. Zhu, M. Bouhrara and J.-M. Basset, *Chem. Rev.*, 2011, **111**, 3036–3075.
26 J. Zheng, Y. Dong, W. Wang, Y. Ma, J. Hu, X. Chen and X. Chen, *Nanoscale*, 2013, **5**, 4894–4901.
27 J. Ge, T. Huynh, Y. Hu and Y. Yin, *Nano Lett.*, 2008, **8**, 931–934.
28 Y. Deng, Y. Cai, Z. Sun, J. Liu, C. Liu, J. Wei, W. Li, C. Liu, Y. Wang and D. Zhao, *J. Am. Chem. Soc.*, 2010, **132**, 8466–8473.
29 C. Pereira, A. M. Pereira, C. Fernandes, M. Rocha, R. Mendes, M. P. Fernández-Garcia, A. Guedes, P. B. Tavares, J.-M. Grenéche, J. P. Araújo and C. Freire, *Chem. Mater.*, 2012, **24**, 1496–1504.
30 K. Möller, J. Kobler and T. Bein, *Adv. Funct. Mater.*, 2007, **17**, 605–612.
31 F. Rouquerol, J. Rouquerol and K. Sing, *Adsorption by Powders and Porous Solids*, Academic Press, San Diego, USA, 1999.
32 C. Pereira, J. F. Silva, A. M. Pereira, J. P. Araújo, G. Blanco, J. M. Pintado and C. Freire, *Catal. Sci. Technol.*, 2011, **1**, 784–793.
33 E. Cano-Serrano, G. Blanco-Brieva, J. M. Campos-Martin and J. L. G. Fierro, *Langmuir*, 2003, **19**, 7621–7627.
34 C. Pereira, A. M. Pereira, P. Quaresma, P. B. Tavares, E. Pereira, J. P. Araújo and C. Freire, *Dalton Trans.*, 2010, **39**, 2842–2854.
35 B. Sahoo, K. Devi, S. Dutta, T. Maiti, P. Pramanik and D. Dhara, *J. Colloid Interface Sci.*, 2014, **431**, 31–41.
36 C. Vericat, M. E. Vela, G. Corthey, E. Pensa, E. Cortés, M. H. Fonticelli, F. Ibañez, G. E. Benitez, P. Carro and R. C. Salvarezza, *RSC Adv.*, 2014, **4**, 27730–27754.
37 (*a*) X. Li, X.-H. Zhu, Y. Fang, H.-L. Yang, X. Zhou, W. Chen, L. Jiao, H. Huo and R. Li, *J. Mater. Chem. A*, 2014, **2**, 10485–10491; (*b*) Y. Zhu, J. Shen, K. Zhou, C. Chen, X. Yang and C. Li, *J. Phys. Chem. C*, 2011, **115**, 1614–1619.
38 R. Xiong, Y. Wang, X. Zhang, C. Lu and L. Lan, *RSC Adv.*, 2014, **4**, 6454–6462.
39 C. Fernandes, C. Pereira, A. Guedes, S. L. H. Rebelo and C. Freire, *Appl. Catal., A*, 2014, **486**, 150–158.
40 P. Innocenzi, P. Falcaro, D. Grosso and F. Babonneau, *J. Phys. Chem. B*, 2003, **107**, 4711–4717.
41 R. Al-Oweini and H. El-Rassy, *J. Mol. Struct.*, 2009, **919**, 140–145.
42 J.-P. Gallas, J.-M. Goupil, A. Vimont, J.-C. Lavalley, B. Gil, J.-P. Gilson and O. Miserque, *Langmuir*, 2009, **25**, 5825–5834.
43 A. S. Chong and X. S. Zhao, *J. Phys. Chem. B*, 2003, **107**, 12650–12657.
44 P. Yuan, P. D. Southon, Z. Liu, M. E. R. Green, J. M. Hook, S. J. Antill and C. J. Kepert, *J. Phys. Chem. C*, 2008, **112**, 15742–15751.
45 V. R. Rai and S. Agarwal, *Chem. Mater.*, 2011, **23**, 2312–2316.
46 G. Socrates, *Infrared and Raman Characteristic Group Frequencies*, John Wiley & Sons, Ltd., Chichester, USA, 3rd edn, 1994.

47 J. Kobler, K. Möller and T. Bein, *ACS Nano*, 2008, **2**, 791–799.
48 I. Robinson, L. D. Tung, S. Maenosono, C. Walti and N. T. K. Thanh, *Nanoscale*, 2010, **2**, 2624–2630.
49 U. Tamer, Y. Gündoğdu, İ. Boyacı and K. Pekmez, *J. Nanopart. Res.*, 2010, **12**, 1187–1196.
50 M. Zhang, B. L. Cushing and C. J. O'Connor, *Nanotechnology*, 2008, **19**, 085601.
51 A. Seth and Y. Cai, *US Pat.*, 8021449 B2, 2011.
52 S. Wunder, F. Polzer, Y. Lu, Y. Mei and M. Ballauff, *J. Phys. Chem. C*, 2010, **114**, 8814–8820.
53 M. M. Nigra, J.-M. Haz and A. Katz, *Catal. Sci. Technol.*, 2013, **3**, 2976–2983.